Design of compact wide-field LWIR optics using a single-layer diffractive optical element

M. FAROOQ[1], M. H. ASGHAR[2], M. SALEEM[3,*], Z. IQBAL[1]
[1]*Riphah International University Islamabad, Pakistan*
[2]*National University of Science and Technology, Islamabad, Pakistan*
[3]*Government Graduate College of Science, Wahdat Road, Lahore, Pakistan*

Visual Unmanned Aerial Vehicles (UAV) navigation requires high-resolution cameras with a wide field of view (WFOV) to ensure effective feature matching in acquired imagery. Designing WFOV optics for large-array Long-Wave Infrared (LWIR) sensors presents unique challenges in achieving optimal optical performance using a minimal number of optical components and without relying on active athermalization. This article presents the design of an 84° × 67° field of view (FOV) optical system for a 1280 × 1024 LWIR microbolometer, achieving a modulation transfer function (MTF) of ≥ 0.6 at 20 lp/mm while maintaining barrel distortion below 20%. The design incorporates only three lenses, including a single-layer diffractive optical element (DOE), offering a low-SWaP solution with high contrast and distortion control.

(Received October 12, 2025; accepted June 2, 2026)

Keywords: Optical design, Diffractive optical elements, Wide field of view, LWIR optics, UAV navigation

1. Introduction

Unmanned Aerial Vehicles (UAVs) have revolutionized disaster-response, security, agriculture, and many other domains. Recent advances in artificial intelligence have unlocked the full potential of onboard imaging for visual navigation—covering localization, mapping, obstacle avoidance, visual odometry, and path planning [1]. Visual-navigation pipelines depend on robust feature detection and classification; their accuracy scales with both the number of features in each frame and the ground-sampling distance (GSD) of the camera [2]. Consequently, UAV visual navigation demands high-resolution, wide-field-of-view (WFOV) imaging systems that maximize the number of discernible features in a single image footprint.

Twenty-four-hour missions in security, search-and-rescue, and real-time intelligence call for sensors that operate in all lighting conditions. Long-wave-infrared (LWIR) microbolometers meet this need: they are compact, uncooled, and cost-effective. In the past decade, high-definition (HD) LWIR arrays with smaller pixel pitches have become available, enabling new applications in surveillance, navigation, industrial inspection, autonomous vehicles, and environmental monitoring. Because a larger detector permits a wider FOV without degrading GSD, HD arrays are ideal for WFOV optics.

Designing high-resolution LWIR cameras is, however, challenging. Refractive optics in the 8–14 µm band tend to be bulky, heavy, and chromatically aberrated owing to the limited choice of infrared materials. Diffractive optical elements (DOEs) alleviate these issues: their strong, negative dispersion lets a designer suppress axial and lateral chromatic aberration while simultaneously correcting distortion [3, 4]. In purely refractive WFOV designs distortion and thermal defocus are especially troublesome [5, 6]; DOEs offer the necessary extra degrees of freedom [7].

A single-layer DOE sacrifices efficiency when the operating wavelength drifts away from its design wavelength [8, 9]. Multilayer DOEs can broaden the bandwidth [10-13] but at the cost of greater fabrication complexity and higher price. Much of the recent literature therefore explores aspheres, special glass combinations, or single-layer DOEs to balance performance, size, weight, and power (SWaP) [13-16].

A selection of earlier WFOV infrared objectives is summarised in Table 1 [16-22].

Typical designs either restrict the FOV (< 70°) or use small detector formats, limiting their suitability for visual-navigation tasks that require ≥ 70° diagonal coverage [23, 24]. To the best of the authors' knowledge, no published work reports an FOV ≥ 80° on a 1280 × 1024 LWIR microbolometer with a 12 µm pixel pitch.

Contribution of this work:

1. Ultra-wide FOV on an HD detector – We present an 84° × 67° objective for a 1280 × 1024, 12 µm LWIR microbolometer, well aligned with visual-navigation requirements.
2. Three-element, low-SWaP design – The lens stack comprises only two refractive elements plus a single-layer DOE, yielding low mass, small volume, and high transmission.
3. Passive thermal robustness – The layout maintains ≥ 0.6 MTF at 20 lp/mm and distortion ≤ 20 % across the full -40 °C to +60 °C range without active athermalisation, further reducing power draw.

4. Benchmarked against a five-element reference-
5. A conventional five-lens WFOV solution was first optimised to the diffraction limit and then distilled into the present three-element form, demonstrating that the DOE can recover image quality while halving the element count.
6. The proposed three-element design has a Nyquist frequency of 41.7lp/mm whereas the 5-lens design has a Nyquist frequency of 33.3 lp/mm. the 3-lens design can determine the frequencies below 41.7lp/mm leading to a resolution of 25% finer details.
7. The proposed 3-lens design has 56% more pixels per unit area than 5-lens design, hence collects 10% more signal per unit area.

The detailed optical prescription, DOE design, and tolerance analysis are discussed in Sections 2–5. Section 3 examines the diffraction efficiency of the single-layer DOE; Section 4 reports image-quality metrics; and Section 5 summarises the conclusions.

Table 1. Representative wide-FOV infrared objectives in the literature

Sr #	**References**	**Spectral Band**	**Sensor Format**	**Pixel Pitch (μm)**	**F#**	**FOV**	**Distortion**
1	Bian et al. [16]	Visible	0.45-in CCD	—	2.0	128	0.9 %
2	Chen et al. [17]	LWIR	640 × 512	20	1.0	40° × 30°	6.1 %
3	Aboalia et al. [18]	LWIR	640 × 512	15	1.0	18°	—
4	Mowafy et al. [19]	LWIR	384 × 288	25	1.4	5.5° × 4.1°	—
5	Ok & Park [20]	LWIR	384 × 288	25	1.44	51.3° × 38.6°	—
6	Curatu [21]	LWIR	320 × 240	25	1.1	24°	5 %
7	Schifano et al. [22]	LWIR	1024 × 768	17	1.0	70°	18.85 %
8	Proposed Design	LWIR	1280 × 1024	12	1.17	84° × 67°	19.8 %

2. Proposed optical design

The objective of the proposed design is to realize an ultra-wide-field (84 ° × 67 °) lens for a 1280 × 1024-pixel LWIR micro-bolometer while minimizing size, weight, and power (SWaP). A single-layer diffractive optical element (DOE) is introduced to shrink the element count and suppress residual aberrations. For benchmarking, a conventional all-refractive objective offering the same FOV was also created without limiting the number of elements. Lens data of the reference (benchmarked) design and proposed design is shown in Table 2 and Table 3 and the key specifications are compared in Table 4.

2.1. Optical layout and materials

The final lens stack (Fig. 1b) contains three elements:
1. G1 (Ge) – positive, spherical
2. G2 (Ge) – positive, aspheric (4^{th}–10^{th} order)
3. G3 (BD-1 chalcogenide) – positive, bianary2; the rear surface carries a single-layer DOE

Only two infrared glasses —germanium and BD-1 — are used, reflecting the limited material palette in the 8–12 μm band. The back-working distance (≈ 10 mm) is ample for a mechanical focus mechanism or protective window. The total track length is held to 56 mm, aiding integration in SWaP-constrained gimbals.

2.2. Diffractive-surface model

Diffractive optical surfaces can be as binary 1, binary 2 or binary 4. The design and optimization process has been carried out using Zemax Optics Studio [25]. Binary 2 surface has been selected, which is similar to the extended asphere surface with an additional polynomial term representing the variation in phase across the optical surface. Sag of the binary 2 surface is similar to the even asphere surface with an added phase according to the following polynomial expansion [25].

$$z(r) = \frac{cr^2}{1+\sqrt{1-(1+k)c^2r^2)}} + \sum_{i=1}^{m} a_{2i}r^{2i}\, a_i\, r^{2i} + m\sum_{i=1}^{N} A_i\rho^{2i} \quad (1)$$

where c is the curvature, k the conic constant, a_{2i} the even-asphere coefficients, m the diffraction order (here **+1**), A_j the DOE polynomial coefficients, and ρ the normalized radius. The optimized coefficients are listed in Table 4 gimbals.

Table 2. Lens prescription data of the reference design

Surf Type	Radius	Thickness	Material	Clear Diam	Conic
OBJ STANDARD	Infinity	Infinity		0	00
STANDARD	Infinity	0		0	0
EVEN ASPHERE	24.760	4.00	Germanium	13.069	-6.252
STANDARD	16.173	13.184		10.445	0
STANDARD	312.963	3.50	Germanium	10.828	0
STANDARD	-103.055	5.20		10.784	0
STANDARD	-80.590	4.00	Germanium	8.553	13.379
STANDARD	-56.705	5.760		8.740	0
STANDARD	-462.482	3.550	Germanium	10.194	0
STANDARD	-74.526	2.712		10.407	0
STANDARD	62.601	3.00	ZnSe	9.843	0
EVEN ASPHERE	54.836	9.261		9.370	6.619
(aper) STANDARD	Infinity	1.000	Germanium	14.000	0
(aper) STANDARD	Infinity	1.360		14.000	0
IMAGE STANDARD	Infinity	-	-	12.300	0

Table 3. Lens prescription data of the proposed design

Surf Type	Radius	Thickness	Material	Clear Diam	Conic
OBJ STANDARD	Infinity	Infinity		0	00
STANDARD	Infinity	0		0	0
EVEN ASPHERE	44.339	2.840	Germanium	13.370	-1.313
STANDARD	13.751	23.769		10.779	0
STOP STANDARD	Infinity	0.680		11.669	0
STANDARD	36.456	3.200	Germanium	11.796	0
STANDARD	98.322	9.521		11.338	0
EVEN ASPHERE	47.764	3.110	BD-1	7.870	-1.916
BINARY 2	111.117	10.580		7.666	155.699
(aper) STANDARD	Infinity	1.000	Germanium	12.000	0
(aper) STANDARD	Infinity	1.800		12.000	0
IMAGE STANDARD	Infinity	-	-	9.800	0

Table 4. Design specifications and performance

Parameter	Reference Design	Proposed Design
Spectral region	8.0 –12 .0 µm	8.0 –12.0 µm
Detector Format	1280 × 1024	1280 × 1024
Pixel Pitch	15 µm	12 µm
Active Area	19.20 mm × 15.36 mm	15.36 mm × 12.29 mm
Image Height	12.29 mm	9.84 mm
Optics F-number	1.23	1.17
Focal Length	12.97 mm	11.05 mm
Field of view	84.82° × 67.85°	84.56° × 67.65°
Track Length	56.50 mm	56.00 mm
On-axis MTF @ 20 lp/mm	FFT: 0.63	FFT: 0.68
Barrel Distortion	24.97 %	19.80 %
80 % Encircled-Energy Radius	72 %	78 %

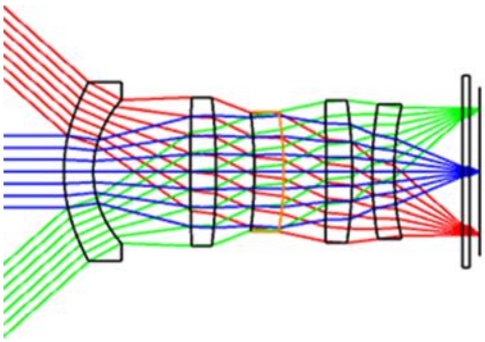

(a)

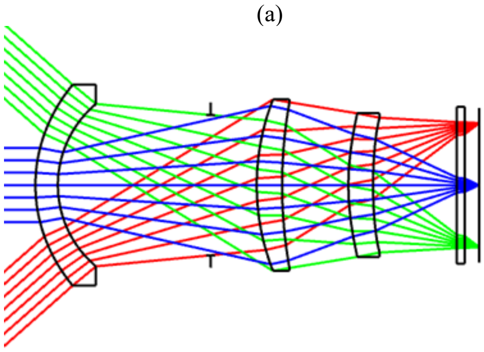

(b)

Fig. 1. Three-dimensional optical design layouts (a) five-element reference design and (b) three-element proposed design (colour online)

2.3. Performance summary

- Resolution: ≥ 0.68 MTF at 20 lp mm⁻¹ on-axis; ≥ 0.60 at full field.
- Distortion: limited to ≤ 20 % across the 84° × 67° field.
- Transmission: improved by ~7 % (fewer air-glass interfaces).
- Thermal stability: focus shift < 15 µm over −40°C to +60°C without active athermalization.

Table 5. Single layer DOE coefficients

Parameter	**Specifications**
Diffraction order *m*	+1
Even-asphere coefficients (6^{th}, 8^{th}, 10^{th})	-5.595×10^{-9}, 1.206×10^{-10}, -9.466×10^{-13}
Maximum term #	05
Normalization Radius	11.500 mm
DOE polynomial (p^2, p^4, p^6, p^8, p^{10})	-44.841, 162.899, -1027.900, 2886.311, -2802.543

These results confirm that a single-layer DOE, paired with only two germanium lenses, can deliver the image quality and FOV required for vision-based UAV tasks while meeting aggressive SWaP targets. Detailed tolerance analysis, stray-light prediction, and diffraction-efficiency calculations follow in Sections 3–5.

3. Single Layer-Diffractive Optical Element (SLDOE)

Rotationally symmetric diffractive optical elements (DOEs) redistribute incident light into multiple diffraction orders [26]. By tailoring the surface-relief phase profile, the designer can concentrate nearly all of the energy into a single order, maximizing efficiency. Fig. 2 illustrates the concept of a continuous-relief single-layer DOE.

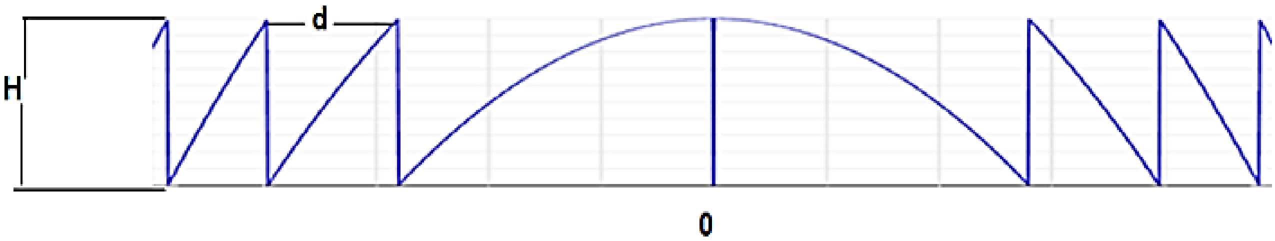

Fig. 2. Schematic structure of a single-layer diffractive optical element (colour online)

3.1. Maximum diffraction efficiency

Maximum diffraction efficiency of a single layer DOE can be calculated from the phase function as [26]

$$\eta(\lambda) = sinc^2\left(\frac{\Phi(\lambda)}{2\pi} - 1\right) \quad (2)$$

With $sinc(x) = \frac{Sin(\pi x)}{\pi x}$, Φ is phase distribution function and λ is design wavelength. The phase function of a single-layer diffractive optical element (DOE) describes how the phase of light changes as it passes through the element. A DOE typically manipulates the phase of light at different points in a structured pattern to produce specific diffraction effects. For a single-layer diffractive optical element, the phase function is typically a function of position in the plane of the DOE. The phase distribution function can be calculated as follows:

$$\Phi(\lambda) = \frac{2\pi H}{\lambda}[n(\lambda) - 1] \quad (3)$$

where $n(\lambda)$ is the refractive index of substrate material and H is the maximum relief depth of microstructure. The optimum groove depth that yields 100 % first-order efficiency at the design wavelength λ_0 is obtained by setting the *sinc* argument to zero, giving [27].

$$H_{opt} = \frac{\lambda_0}{n(\lambda_0) - 1} \quad (4)$$

Substituting the value of $\Phi(\lambda)$ from equation (3) into equation (2) diffraction efficiency can be calculated.

3.2. Design example

In the present lens the DOE is blazed for λ_0 = 10.0 µm (centre of the 8–12 µm LWIR band). Germanium's dispersion is modest but non-negligible:

n(8 µm) ≈ 4.0046, n(10 µm) ≈ 3.996

Using Eqs. (3)–(4), the calculated first-order efficiency is

- η(10 µm) ≈ 100 % (by construction),
- η(8 µm) ≈ 97.6 %,

indicating that only a small fraction of energy leaks into undesired orders across the operating band. This residual loss has a negligible effect on image quality, as confirmed in Section 4 [19, 20].

3.3. Optimization strategy

In the lens was re-optimized with the DOE in place, subject to constraints on

- effective focal length,
- total track length (first surface to image plane),
- working f-number.

A damped-least-squares algorithm minimized a merit function comprising the RMS spot radius and the root-mean-square (RMS) wavefront error [25]. These criteria ensured diffraction-limited (or near-diffraction-limited) performance while preserving the system's low-SWaP goals.

4. Optical performance evaluation

In order to verify the overall performance of a system, diagnostic tools like modulation transfer function (FFT/Huygens), RMS spot diagram, Optical path differences, field curvature, distortion and encircled energy have been utilized.

4.1. Modulation Transfer Function (MTF)

The MTF quantifies how faithfully contrast is transferred from object to image as a function of spatial frequency; higher values indicate better contrast reproduction. The Nyquist frequency for 1280 × 1024 sensor with 12 µm pitch can be calculated as fallows

$$f_{Nyq} = \frac{1}{2p} = \frac{41.7lp}{mm} \quad (5)$$

It means frequencies below 41.7 lp/mm will determine usable feature contents in the image. The optical cutoff frequency of the lens is

$$f_{cutoff} = \frac{1}{\lambda F\#} \quad (6)$$

Considering the design wavelength λ = 10 µm and F#=1.17, the cutoff frequency isd

$$f_{cutoff} = 85.5lp/mm$$

As $f_{cutoff} \gg f_{Nyq}$, therefor any improvement in the MTF, PSF, Wavefront error or distortion will directly affect the image quality. MTF can be considered as feature preservation curve. It means even a small improvement in MTF will result in higher image contrast and better feature detectability.

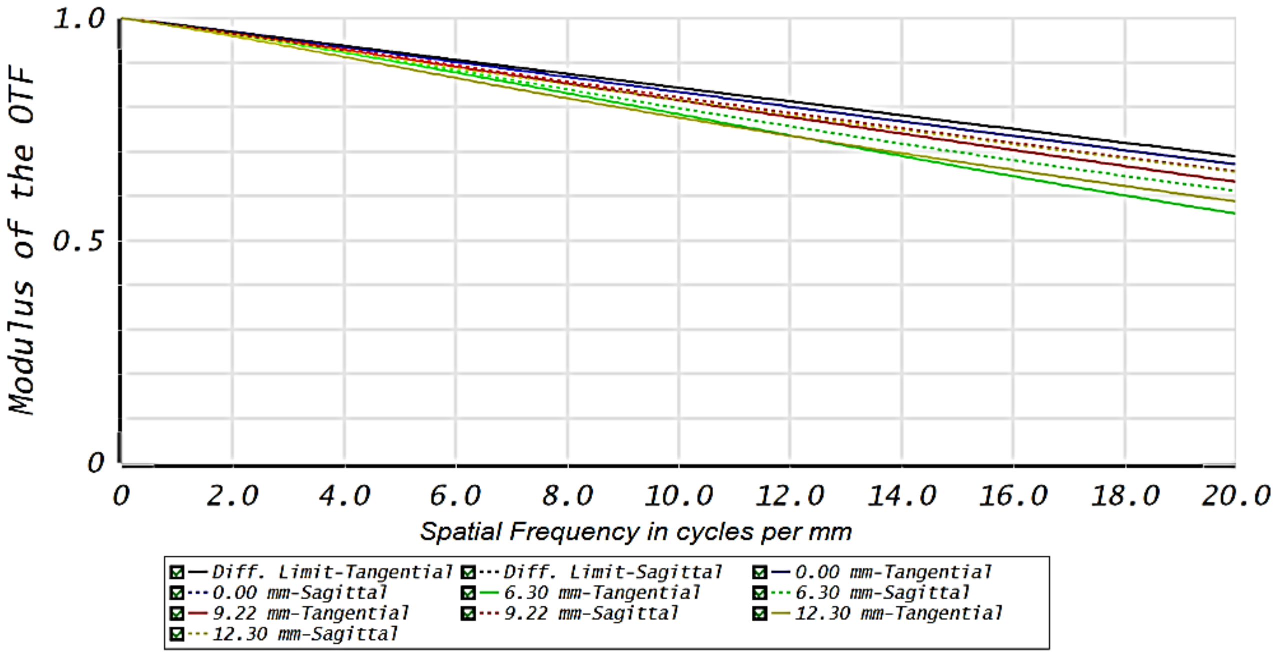

(a)

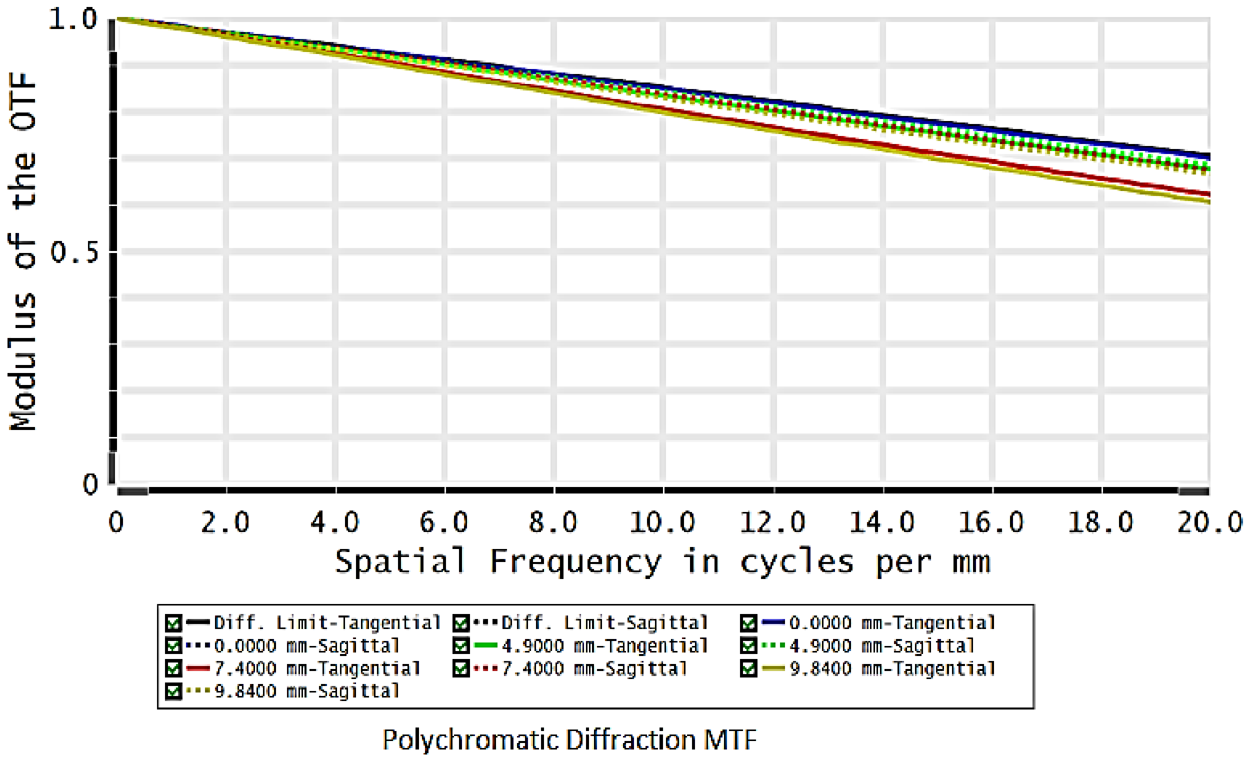

(b)

Fig. 3. MTF versus field position: (a) five-element reference; (b) three-element proposed design (colour online)

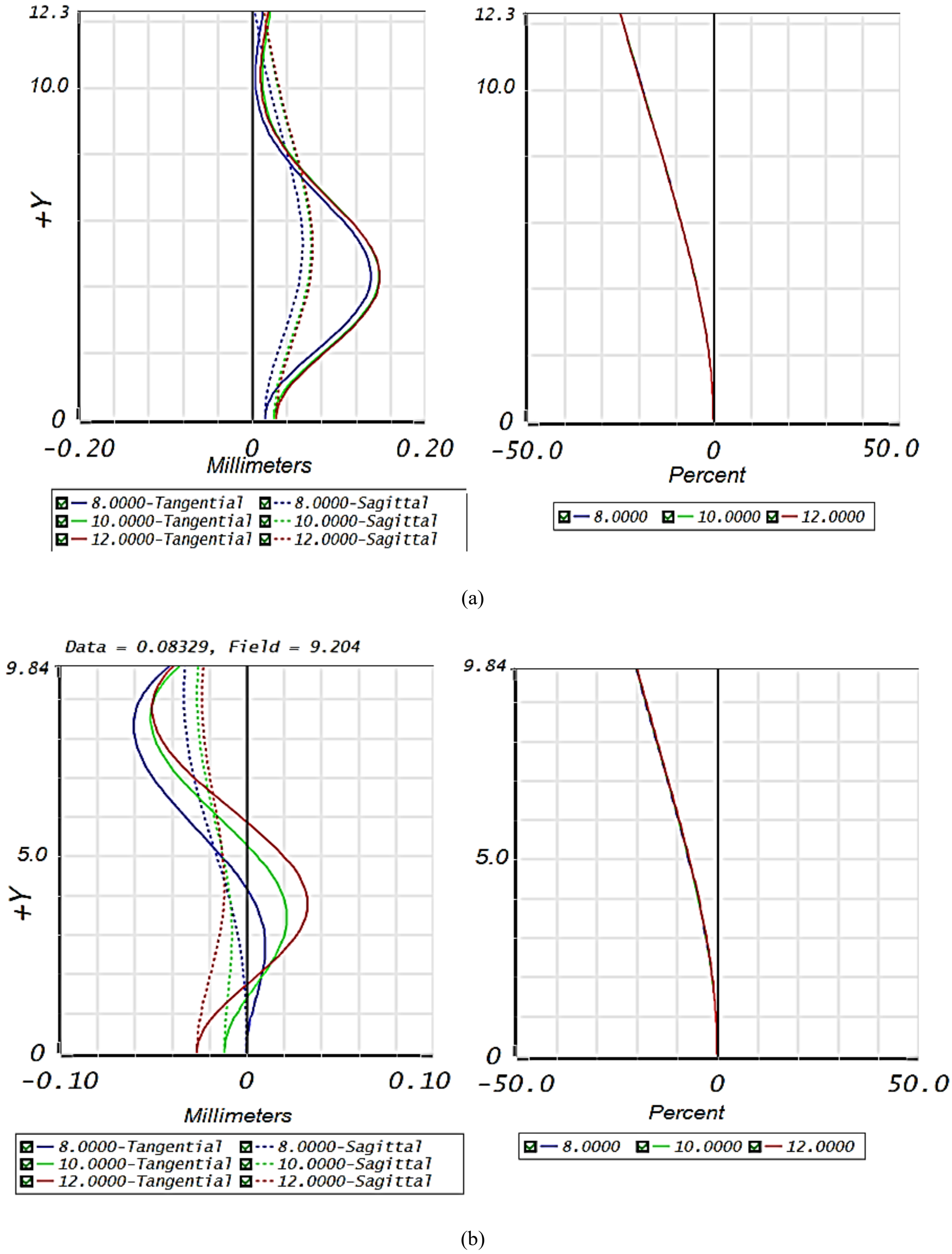

Fig. 4. Field curvature & distortion (a) reference design and (b) proposed design (colour online)

Fig. 3 compares the MTF of the two designs. The proposed three-element lens is diffraction-limited on-axis, and across 0.5, 0.75, and full field it maintains MTF ≥ 0.60 at 20 lp/mm - comfortably above the 0.4–0.5 benchmark for high-quality LWIR objectives [16, 27]. The full axis MTF of the proposed system is more than 12 % improved as compared to the conventional 5-lens design at 20 lp/mm leading to significant reduction in effective point spread function width at the edge of the field. For a 12 µm pixel sensor, this corresponds to a desirable reduction in feature localization uncertainty leading to reduced reprojection errors and cumulative pose drift.

4.2. Field curvature and distortion

The field curvature (FC) is an image anomaly which degrades the image if sagittal and tangential image do not coincide on a single plane, which is usual case in almost all imaging systems. Field curvature increases with increase in image height at lower focal lengths as square of image height divided by focal length (FC = $-h^2/f$) [28]. The field curvature plots show the corrected curvatures at full filed within the range [29]. Distortion is a rotationally symmetric image error which increases from the center of the image towards the edges. This modifies the image scale within the image plane, which can be very disturbing for measuring applications. The visual odometry (VO) and vision-aided Navigation (VAN) employes feature descriptors for feature matching in sequential camera frames on moving camera. The feature descriptors assume that localized image fallow affine transforms. The distortion in imaging system causes non-affine image warping introducing scale and orientation errors resulting in fewer matches. It is observed that even small distortion may result in systematic position bias with increased errors at patches away from the center of the image. The improvement in the field curvature of the proposed 3-lens design leads to a measurable increase in MTF at off-axis field points, with up-to a 15-20% contrast gain at 15-20lp/mm near the image periphery compared to the 5-lens design. The improved field curvature of the proposed design will lead to better sharpness consistency from the image center to the periphery and special feature such as edges, corners, and textured regions are expected to be preserved with similar contrast. And high frequency image contents for all field points. As a result, the proposed DOE based design is expected to produce high feature retention across the field of view and lower reprojection errors leading to improved robustness of feature matching algorithms. Using diffractive surface, the distortion has been reduced to less than 20%. Field curvature and distortion curves are shown in Fig. 4 above.

4.3. Standard spot diagram and optical-path difference curves

Spot diagram is the blurriness of a point source (object) formed by the system. Resolution of any systems depends upon the blur diameter and single pixel size. The RMS spot diameter is the diameter of a circle containing approximately 68% of the energy [6]. The spot size should be of comparable scale to pixel size. Fig. 5 shows the RMS spot size for all fields (on axis, 0.5, 0.75 and full field).

Optical path difference (OPD) is extremely useful parameter for performance evaluation of imaging systems. If P-V of an OPD is less than or equal to quarter wavelength then the image will be comparable to the perfect [6]. OPD errors shown in Fig. 6 are in closes agreement as per Rayleigh’s law of diffraction limited system.

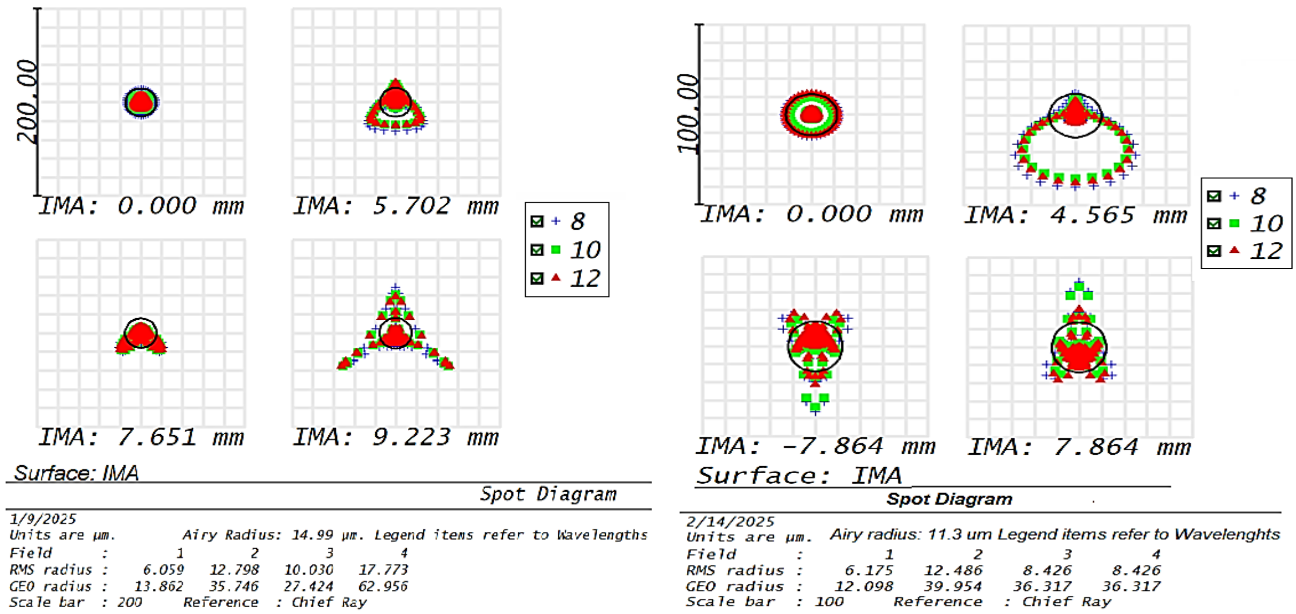

(a) (b)

Fig. 5. Standard spot diagrams at 8, 10, and 12 µm: (a) SPD reference design (b) SPD proposed design (colour online)

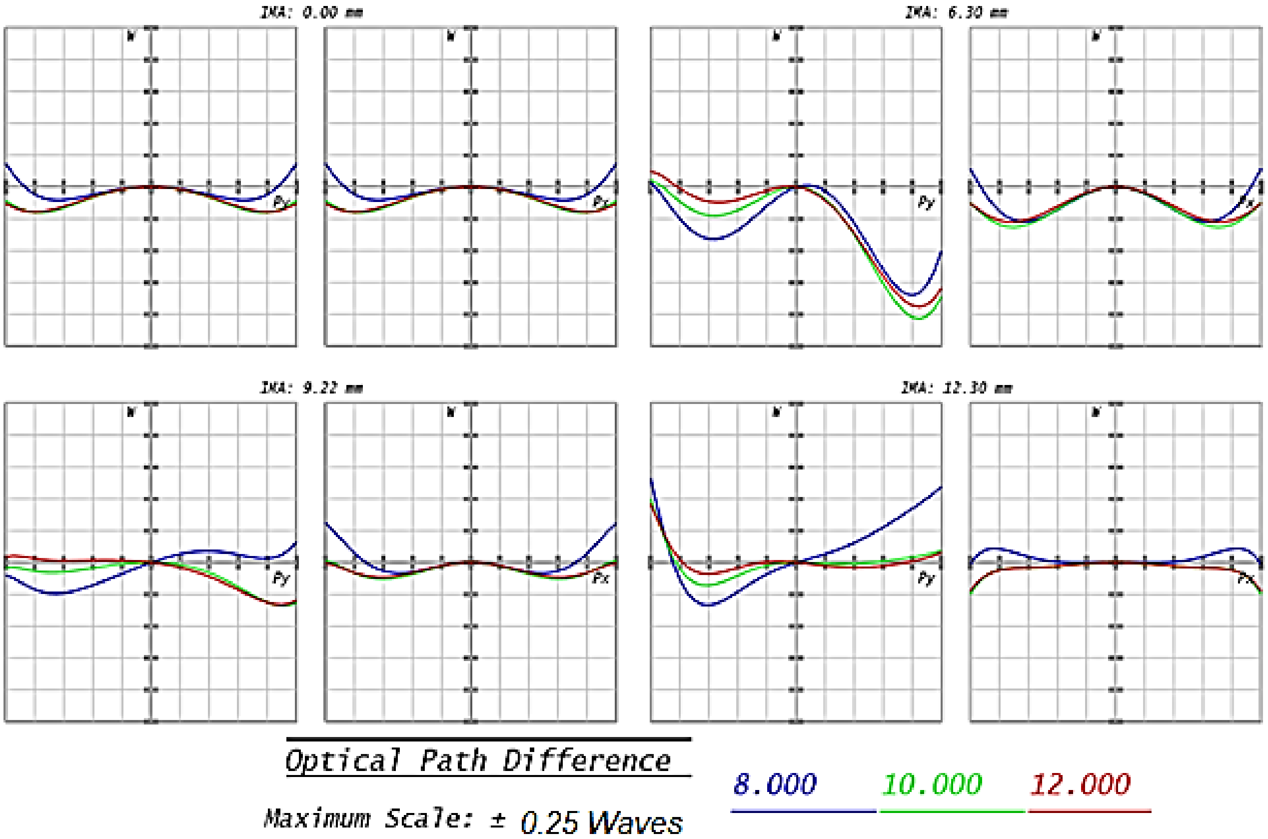

(a)

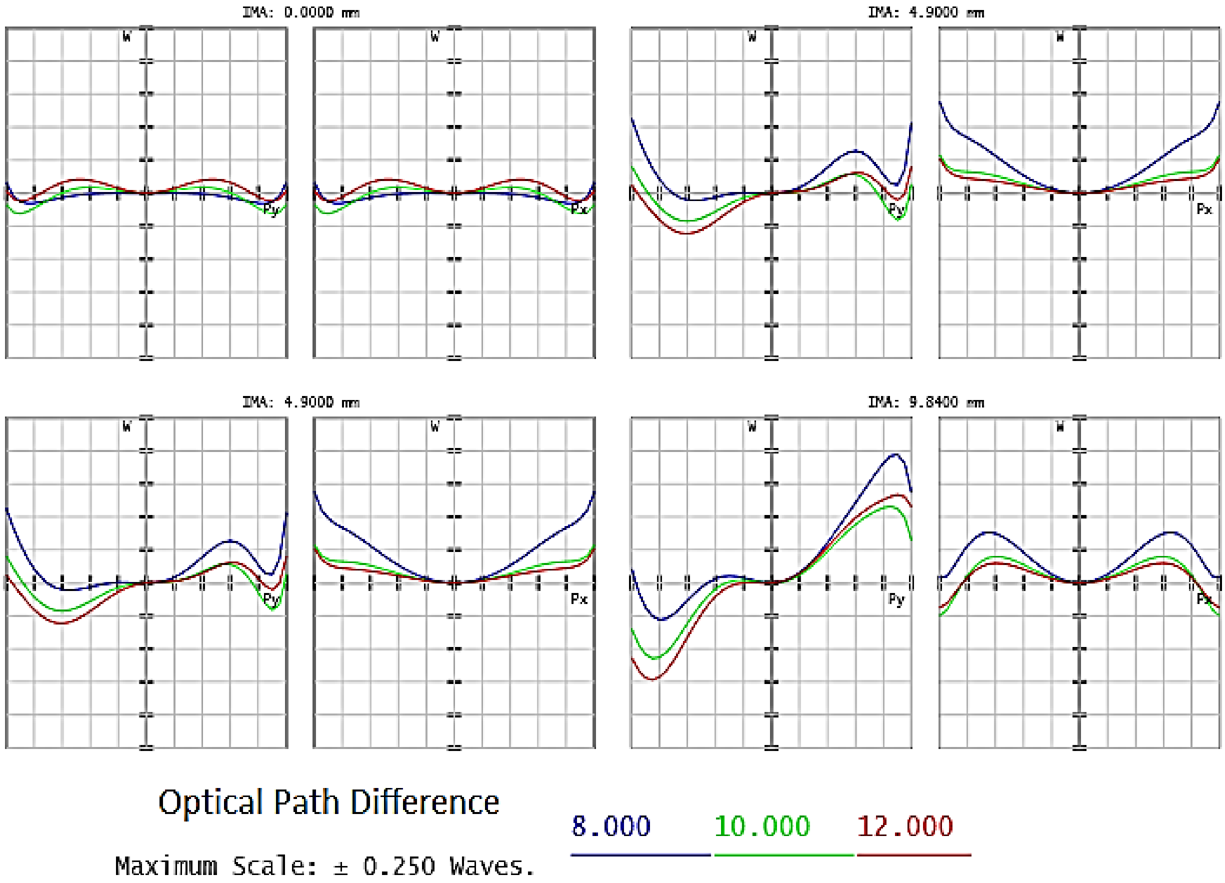

(b)

Fig. 6. Optical path difference maps (a) reference design (b) proposed design (colour online)

4.4. Encircled-energy criterion

Encircled energy is the energy percentage plotted as a function of image diameter. For good reliable system, at least 80% of the energy from a point source (object) should fall within the diameter of the pixel [6]. Fig. 7 shows that the three-element design meets this 80 %-within-12 μm requirement across the entire 84° × 67° field, while the reference lens only marginally satisfies it at the edges.

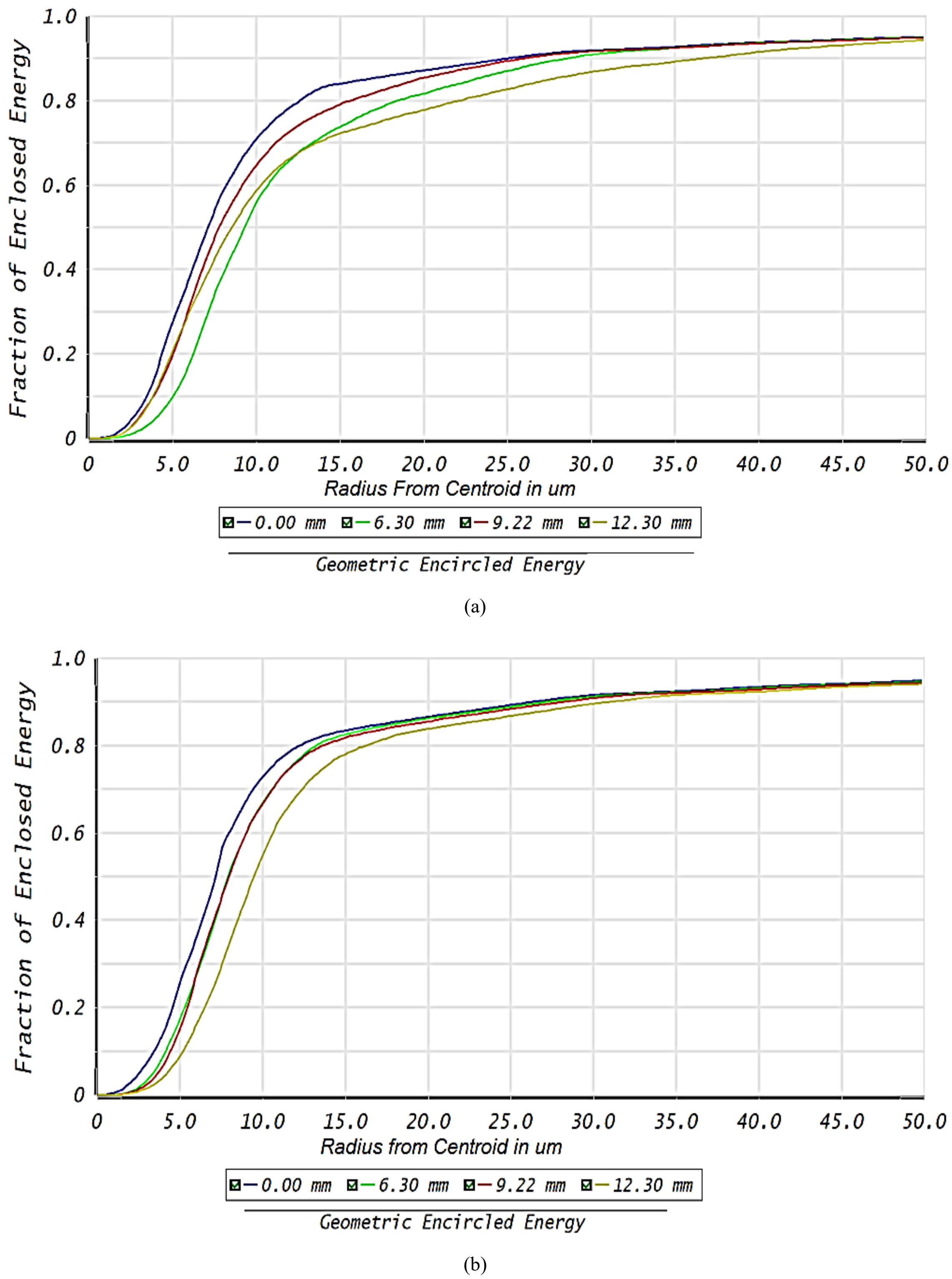

(b)

Fig. 7. Encircled-energy versus image-radius: (a) reference; (b) proposed (colour online)

5. Conclusion

We have demonstrated a compact, three-element LWIR objective that achieves an ultra-wide field of view by integrating a single-layer diffractive optical element (SL-DOE). Reducing the element count from five to three delivers multiple benefits:

- Optical quality — Barrel distortion is held below 20 %, and the lens maintains MTF ≥ 0.60 at 20 lp/mm across the 84 ° × 67 ° field.
- Aberration control — The SL-DOE compensates chromatic and geometric aberrations that are difficult to balance in purely refractive wide-angle designs.
- Low SWaP — Fewer elements translate into lower mass, a shorter 56 mm track length, and higher transmission—improving both image brightness and thermal stability.
- Cost and manufacturability — Using just two common IR materials (Ge and BD-1) and a single Layer DOE keeps production complexity and price in check.

Overall, the proposed lens meets or surpasses the performance targets required for vision-based UAV navigation, where wide coverage and high contrast are essential for reliable feature detection, mapping, and obstacle avoidance. The approach offers a practical, scalable path to high-performance LWIR optics in other size-, weight-, and power-constrained platforms as well.

Disclosures

The authors declare no conflicts of interest.

Acknowledgement

The authors thankfully acknowledge the support of Riphah International University Islamabad, Pakistan for providing resources to conduct this research work.

References

[1] M. Y. Arafat, M. M. Alam, S. Moh, Drones **7**, 89 (2023).
[2] V. Gay-Bellile, A.-C. Escher, D. Salos, L. Soulier, L. Deambrogio, C. Macabiau, IET Radar, Sonar & Navigation **8**, 1059 (2014).
[3] D. C. O'Shea, T. J. Suleski, A. D. Kathman, D. W. Prather, Diffractive optics: Design, Fabrication, and Test (SPIE Vol. **TT62**), SPIE- International Society for Optical Engineering, 2003.
[4] L. Yang, C. Liu, S. Li, Applied Optics **56**, 4532 (2017).
[5] B. Zhang, Q. Cui, M. Piao, Y. Hu, Optics Communications **415**, 156 (2018).
[6] R. Fischer, B. Tadic, Optical system design. McGraw-Hill Education, 2000.
[7] Y. Soskind, Proceedings of SPIE - The International Society for Optical Engineering **9451** (2015).
[8] C. Xue, Q. Cui, T. Liu, L. Yang, B. Fei, Opt. Lett. **35**, 4157 (2010).
[9] B. Zhang, K. Dong, M. Piao, J. Wang, R. Jia, H. Jiang, Optics Communications **502**, 127340 (2022).
[10] Y. Hu, Q. Cui, L. Zhao, M. Piao, Opt. Express **26**, 26845 (2018).
[11] B. Zhang, Q. Cui, M. Piao, Y. Hu, Applied Optics **58**, 2058 (2019).
[12] V. Laborde, J. Loicq, J. Hastanin, S. Habraken, Applied Optics **61**, 7415 (2022).
[13] Z. Bo, C. Qingfeng, P. Mingxu, Acta Optica Sinica **40**, 0605001 (2020).
[14] D. J. Reiley, R. A. Chipman, Applied Optics **31**, 2188 (1992).
[15] B. Hristov, SPIE Optical Design and Engineering IV **8167**, 81670D (2011).
[16] Y. Bian, H. Li, Y. Wang, Z. Zheng, Applied Optics **54**, 8241 (2015).
[17] J. Chen, J. Su, N. Jin, Z. Li, X. Zhang, H. Zhang, L. Zhou, Applied Sciences **7**, 1195 (2017).
[18] H. Aboalia, S. Hussein, A. Mahmoud, 14th International Conference on Electrical Engineering (ICEENG), pp. 66-71 (2024).
[19] K. Mowafy, T. El-Dessouky, M. Medhat, Journal of Optics **52**, 281 (2023).
[20] C.-M. Ok, S.-C. Park, Journal of the Optical Society of Korea **18**, 574 (2014).
[21] G. Curatu, Proceedings of SPIE - The International Society for Optical Engineering (2008).
[22] L. Schifano, L. Smeesters, F. Berghmans, Sensors **21**, 4444 (2021).
[23] M. Shugaev, I. Semenov, K. Ashley, 2024 IEEE/CVF Winter Conference on Applications of Computer Vision (WACV) pp. 208 -217 (2024).
[24] J. J. Engel, J. Sturm, D. Cremers, International Conference on Intelligent Robots and Systems, pp. 2815-2821 (2012).
[25] Zemax, "Zemax opticstudio19.4," Ansys Inc. (2019).
[26] B. H. Kleemann, M. Seeßelberg, J. Ruoff, Journal of the European Optical Society **3**, 08015 (2008).
[27] H. Xie, D. Ren, C. Wang, Journal of Modern Optics **65**, 255 (2018).
[28] A. Noor, F. Elshafia, M. Ahmed, Journal of Applied Physics **6**, 32 (2014).
[29] W. J. Smith, Modern Optical Engineering, 4ed. McGraw Hill LLC (2007).

*Corresponding author: muh.saleem@gmail.com